Improving Blue InGaN Laser Diodes Performance with Waveguide Structure Engineering

Zahra Danesh Kaftroudi[*,1]

[1] Department of Engineering Sciences, Faculty of Technology and Engineering
East of Guilan, University of Guilan, Rudsar-Vajargah, Iran

Abstract: To enhance lasers' power and improve their performance, a model was applied for the waveguide design of 400 nm InGaN/InGaN semiconductor laser, which is much easier to implement. The conventional and new laser structures were theoretically investigated using simulation software PICS3D, which self-consistently combines 3D simulation of carrier transport, self-heating, and optical waveguiding. Excellent agreement between simulation and experimental results was obtained by careful adjustment of the material parameter in the physical model. Numerical simulation results demonstrate that the new waveguide structure can efficiently increase the output power, lower the threshold current, and improve the slope efficiency, which is simply applicable to any kind of InGaN edge emitting lasers. Flatten band gap in the p-side of the InGaN laser diode in new laser structure resulted in an increase in the hole current density in the quantum well while simultaneously the electron confinement in the active region was effectively created, leading to the increased stimulated recombination rate. Furthermore, optical mode-overlap with heavily p-doped was declined, which is the main reason for a better performance of InGaN laser diode.

Keywords: InGaN Laser Diode, Waveguide Design, Numerical Analysis, PICS3D.

1. INTRODUCTION

Group-III nitride semiconductors have received much attention in the past few years due to their promising applications in the field of optoelectronic devices such as light-emitting diodes (LEDs) used in solid-state lighting and laser diodes (LDs) and in high-density optical storage systems, laser printing, biological agent detection systems, and medicine [1-4].

Common features among the best nitride laser diodes demonstrated to date include a multiple-quantum-well (MQW) active region within a separate confinement heterostructure (SCH) and cladding layers. In addition, a high-

---

[*] Corresponding author. Email: Zahraadaneh@guilan.ac.ir

aluminum-content p-type AlGaN Mg-doped layer is also grown immediately over the quantum wells as an electron-blocking layer (EBL) [5].The purpose of EBLs in an LD epitaxial structure is to prevent the leakage of electrons from the active region. Within the QWs, captured electrons have a tendency to escape because of their small effective mass. In the absence of EBLs, electrons injected from the n-side may reach deep the p-side where they may recombine non-radiatively. The conduction band offset of the EBL tends to block the flow of escaping electrons and, thus, improve the electroluminescence efficiency by reducing non-radiative recombination in the quasi-neutral p-type material above the active region[6].Nevertheless, the interface charge associated with the III-N homogeneous EBLs plunges the conduction energy downward relative to the electron quasi-Fermi level at the spacer/EBL interface [7] and may also lead to a parasitic inversion layer in the p-type spacer materials [8]. Due to the influence of non-radiative recombination processes, the formation of this parasitic inversion layer leads to a reduction in optical gain. Furthermore, homogeneous EBLs also give rise to the undesirable hole blocking layers on the p-side [9, 10], exacerbating the problem of hole injection. If the bandgap energy of EBLs is widened with the intention of blocking more electrons, the overall situation becomes aggravated because more polarization charges are introduced at the EBL/spacer interface [6]. Another problem that exists in nitride laser with EBL is the difficulty of AlInN epitaxially growth with superior crystalline quality because of the disparity in the optimum growth temperature between AlN and InN [6]. Highly conductive p-type layers (waveguide and EBL) are essential to efficiently inject holes into the active region of LDs. However, the conductivity of p-type III-N materials is usually inferior to that of the n-type materials. This lower conductivity is primarily due to the limited p-type doping efficiency because of the high activation energy of Mg dopant atoms and possibly other compensation mechanisms [11-13].The situation worsens approaching wider bandgap materials. The poor conductivity of p-type layers in LD designs has several consequences. Joule heating may necessitate the operation of LDs in pulsed mode instead of continuous wave (CW) mode. A large fraction of the applied voltage may be dropped across the p-waveguide and EBL because of the parasitic series resistance. This voltage drop may reduce the effectiveness of the EBL to block the leakage of electrons from the active region as a result of band bending. The artificial hole blocking layers may emerge on the p-side at the waveguide/EBL and EBL/spacer interfaces, limiting the mechanism for hole injection to inefficient thermionic emission [6].

To mitigate the deleterious effects, various approaches are now the focus of intensive research [14-15]. Modern semiconductor laser design approaches extensively use different structure designs in order to improve characteristics of

laser diodes. A simple way to optimize laser performance is the waveguide design engineering. Numerous studies have been reported on the performance of laser diodes with different waveguide structure designs [16]. To achieve sufficient electron confinement without using the AlGaN EBL in Group-III nitride semiconductor laser, a new waveguide structure can be employed. In this design, MQW is located immediately adjacent to the p-cladding layer and displaced from the center of the waveguide [17].

Here, first, the conventional InGaN multi-quantum well laser (MQW) with AlGaN EBL is simulated theoretically using PICS3D, which self-consistently combines 3D simulation of carrier transport, self-heating, and optical wave-guiding. Excellent agreement between simulation and measurement is obtained by careful adjustment of the material parameter in the model. The laser structure and experimental results were reported by Nakamura [18]. Second, the effect of the new waveguide structure on the conventional InGaN laser performance is investigated. The output power, threshold current and optical intensity and the electric field of InGaN laser are also obtained and compared with conventional InGaN structure.

The laser structure and physical models are introduced in Section 2. The material parameters used in this work and comparison with experimental results are presented in Section 3. The simulation results and discussion are given in Section 4.

2. LASERS STRUCTURES AND THEORETICAL MODEL

In this simulation, the InGaN laser structure consisted of a 3 µm thick layer of n-type GaN, a 0.1 µm thick layer of n-type $In_{0.05}Ga_{0.95}N$, a 0.5 µm thick layer of n-type $Al_{0.08}Ga_{0.92}N$, a 0.1 µm thick layer of n-type GaN, three 35 A° thick Si-doped $In_{0.15}Ga_{0.85}N$ well layers, four 70 A° thick Si-doped $In_{0.02}Ga_{0.98}N$ barrier layers, a 200 A° thick layer of p-type $Al_{0.2}Ga_{0.8}N$, a 0.1 µm-thick layer of p-type GaN, a 0.5 µm thick layer of p-type $Al_{0.08}Ga_{0.92}N$, and a 0.3 µm thick layer of p-type GaN. The 0.1 µm thick n-type and p-type GaN layers were light-guiding layers. The 0.5 µm thick n-type and p-type $Al_{0.08}Ga_{0.92}N$ layers acted as cladding layers for the confinement of the carriers and the light emitted from the active region of the InGaN MQW structure. The area of the ridge-geometry LD was 4 µm × 150 µm. High-reflection facet coatings (50%) consisting of quarter-wave TiO–SiO dielectric multilayers were used to reduce the threshold current [18]. The structure of the InGaN MQW laser is shown in Fig. 1.
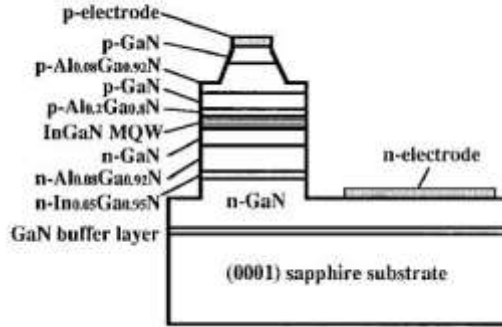
Fig. 1. The structure of the InGaN MQW LD's [17].

The numerical simulation in the present work was executed using the PICS3D program, which can be applied to assess the optimization of the existing devices by calibration of a specific material [19]. In this program, the valence-band structure, which included the coupling of the heavy-hole (HH), the light-hole (LH), and the spin-orbit split-off bands, was calculated by a 6×6 Hamiltonian with envelope function approximation (k.p approximation) [20-23].

$$H_{6\times6} = \begin{bmatrix} H^U & 0 \\ 0 & H^L \end{bmatrix} \tag{1}$$

$$H^U = \begin{bmatrix} F & K_t & -iH_t \\ K_t & G & \Delta - iH_t \\ iH_t & \Delta + iH_t & \lambda \end{bmatrix} \tag{2}$$

$$H^L = \begin{bmatrix} F & K_t & iH_t \\ K_t & G & \Delta + iH_t \\ -iH_t & \Delta - iH_t & \lambda \end{bmatrix} \tag{3}$$

$$F = \Delta_1 + \Delta_2 + \lambda + \theta$$

$$G = \Delta_1 - \Delta_2 + \lambda + \theta$$

$$\lambda = \frac{\hbar^2}{2m_0}(A_1 K_z^2 + A_2 K_t^2) + \lambda_\varepsilon$$

$$\lambda_\varepsilon = D_1 \varepsilon_{zz} + D_2(\varepsilon_{xx} + \varepsilon_{yy})$$

$$\theta = \frac{\hbar^2}{2m_0}(A_3 K_z^2 + A_4 K_t^2) + \theta_\varepsilon$$

$$\theta_\varepsilon = D_3 \varepsilon_{zz} + D_4(\varepsilon_{xx} + \varepsilon_{yy})$$

$$K_t = \frac{\hbar^2}{2m_0} A_5 K_t^2$$

$$H_t = \frac{\hbar^2}{2m_0} A_6 K_z K_t$$

$$\Delta = \sqrt{2}\Delta_3 \tag{4}$$

$$K_t^2 = K_x^2 + K_y^2 \tag{5}$$

The optical gain mechanism in InGaN quantum wells of real lasers is not yet fully understood. It may be strongly affected by a non uniform Indium distribution. Internal polarization fields tend to separate quantum-confined electrons and holes, thereby reducing optical gain and spontaneous emission. However, screening by electrons and holes is expected to suppress quantum well polarization fields at a high-power operation. The high carrier concentration also eliminates excitons [24]. Considering all the uncertainties in the gain calculating of real InGaN quantum wells, a simple free-carrier gain model including a Lorentzian broadening function was employed:

$$g(E) = \frac{g_0}{2\pi Et} \sum_{i,j} \int_0^\infty \frac{(\frac{\pi}{\Gamma}) f_{dip}(k_t) M_b (f_j - f_i) d^2 k_t}{1 + \frac{(E_{cj}(k_t) - E_{kpi} - E)^2}{\Gamma^2}} \tag{6}$$

where t is the thickness of the QW and $\Gamma = \hbar / \tau_{scat}$ is the broadening due to intraband scattering relaxation time τ_{scat}. E_{cj} is the j_{th} conduction subband and E_{kpi} is the i_{th} valence sub band from the k.p calculation. The sum is over all possible conduction and valence subbands. $g_0 = \pi q^2 \hbar / \varepsilon_0 c m_0^2 n$ is a constant with all symbols having their usual meanings. M_b is a dipole moment [19].

The illustration of electrical behavior of a GaN laser in this study was governed by Poisson's equation [20]:

$$-\nabla.\left(\frac{\varepsilon_0\varepsilon_{dc}}{q}\nabla V\right) = -n + p + N_D(1-f_D) - N_A + \sum_j N_t(\delta_j - f_{tj}) \tag{7}$$

The current continuity equations for electrons and holes were:

$$\nabla.\mathbf{J_n} - \sum_j R_n^{tj} - R_{sp} - R_{st} - R_{Aug} + G_{opt}(t) = \frac{\partial n}{\partial t} + N_D\frac{\partial f_D}{\partial t} \tag{8}$$

$$\nabla.\mathbf{J_p} + \sum_j R_P^{tj} + R_{sp} + R_{st} + R_{Aug} - G_{opt}(t) = -\frac{\partial P}{\partial t} + N_A\frac{\partial f_A}{\partial t} \tag{9}$$

where V is the electrostatic potential and n and p are the electron and hole concentrations, respectively. $\mathbf{J_n}$ and $\mathbf{J_p}$ denote the carrier flux density. N is the doping impurity where the subscripts D and A are used to denote donor and acceptor, respectively. R represents the recombination rate and G is the generation term. The electron and hole concentrations were defined by Fermi–Dirac distribution and a parabolic density of state. For QWs, the following equations were given to express the density of electrons and holes in a QW [20]:

$$n = \sum_j \rho_j^0 KT\ln\left[1 + e^{(E_{fn}-E_j)/KT}\right] + unconfined\ electrons \tag{10}$$

$$p = \sum_i \rho_i^0 KT\ln\left[1 + e^{(E_i-E_{fp})/KT}\right] + unconfined\ holes \tag{11}$$

where the subscript i denotes all confined states for different hole bands and j denotes those for the Γ and L bands. The number of unconfined carriers was calculated using Fermi– Dirac statistics. For current transport across the junctions, the thermionic emission theory [25], defined by:

$$\mathbf{J}_{hn} = \gamma_{hn}.\overline{V_{bn}^{therm}}(n_b - n_{b0}) \tag{12}$$

$$\mathbf{J}_{hp} = \gamma_{hp}.\overline{V_{bp}^{therm}}(p_b - p_{b0}) \tag{13}$$

is used, where γ_{hn} and γ_{hp} are the correction constants, $\overline{V}$ is the thermal recombination velocity, n_b and p_b denote the electron and hole concentrations on the barrier side of the junction, respectively, and n_{b0} and p_{b0} are the corresponding concentrations when the quasi-Fermi levels are the same as those on the opposite side. These equations ensure that the net current is zero when the quasi-Fermi levels on both sides of the barriers are the same. The quantum

tunneling effect is only taken into account when solving the carrier transport in the multiple quantum well active region; however, it is neglected when solving the carrier transport in the bulk region, including the electron-blocking layer [19].

For the treatment of device heating, the thermoelectric power and the thermal current induced by temperature gradient were solved utilizing the method provided by Wachutka [26]. Various heat sources, including Joule heat, generation/recombination heat, Thomson heat, and Peltier heat, are taken into account in this specific study. The software solved the scalar Helmholtz equation to obtain a transverse component of the optical field. The lateral components were given by Bessel functions. Further details of the model can be found elsewhere [27].

3. MATERIAL PARAMETERS AND COMPARISON TO MEASUREMENTS

The inclusion of correct material parameters is of paramount importance for realistic device simulation. These parameters depend on the material composition and may be different for every layer in the device. Published values sometimes spread over a wide range, and it is difficult to select the number most appropriate for a given device. Therefore a detailed discussion of those material parameters that are crucial for the simulation is included. The parameter calibration process is described in the following section and it leads to good agreement between simulations and measurements [27].

The carrier drift-diffusion model includes Fermi statistics and incomplete ionization of dopants. The high activation energy of the Mg acceptor causes the hole density to be considerably smaller than the Mg density. We applied the Mg activation energy of 170 meV for GaN, which is assumed to increase by 3 meV per % Al for AlGaN. In n-type material, the Si donor activation energy is~20 meV [28].

The carrier mobility is the key material parameter in transport simulations. A widely used empirical expression for modeling the mobility of electrons and holes is the Caughey-Thomas approximation, which was employed in our calculation and can be expressed as [29]:

$$\mu(N) = \mu_{\min} + \frac{\mu_{max} - \mu_{\min}}{1 + (\frac{N}{N_{ref}})^{\alpha}} \tag{14}$$

where $\mu_{\min}$, $\mu_{\max}$, N_{ref}, and α are fitting parameters according to the experimental mobility measurements. We employed this carrier mobility model for binary GaN material in our calculation. The relative parameters are summarized in

Table I [28]. As for ternary AlGaN and InGaN, the analytical expressions for mobility as a function of doping density have been established by Monte Carlo simulation for various nitride alloys [28]. The values in Table I are extracted from this procedure.

TABLE I
G$_{A}$N M$_{OBILITY}$ P$_{ARAMETERS}$

Parameters	μ_{min}	μ_{max}	N_{ref}	α
Unit	cm^{2}V^{1}S	1/cm^{2}VS	1/cm^3	-
electrons	295	1461	1×10^{17}	0.66
holes	3	170	3×10^{17}	2

Defect-related recombination is known to be the main carrier loss mechanism in nitride devices. The Shockley-Read-Hall (SRH) recombination lifetime of electrons and holes was assumed to be 1 ns; however, this is a rough estimate since the type and density of recombination centers are sensitive to the technological process. Within passive layers, a spontaneous emission parameter of B=2×10^{-11} cm^3 s^{-11} was employed [30]. The spontaneous recombination rate in quantum wells is larger than in passive layers and is calculated by integration of the spontaneous emission spectrum. From its bandgap dependence in other materials, a very small Auger parameter of C=10^{-34} cm^6 s^{-1} was estimated for GaN. Thus, even with large carrier densities, Auger recombination in nitride materials is negligible [28].

Thermionic emission is mainly controlled by the offset of the conduction band (ΔE_c) and valence band (ΔE_v) at hetero-barriers. A band offset ratio of ΔE_c / ΔE_v = 0.7/0.3 was assumed for InGaN/GaN as well as for AlGaN/GaN [28]. For unstrained layers with a low mole fraction of the alloy element, we employed the following room temperature relations for the direct bandgap (eV) [28]:

$$E_g(In_xGa_{1-x}N) = 1.89x + 3.42(1-x) - 3.8x(1-x) \tag{15}$$

$$E_g(Al_xGa_{1-x}N) = 6.28x + 3.42(1-x) - 1.3x(1-x) \tag{16}$$

For the design of optical waveguides, the compositional change of the refractive index is often more important than its absolute value. In comparison to refractive index measurements on Al$_x$Ga$_{1-x}$N (x<0.38), the Adachi model was found to be most accurate using fit parameters obtained from measurements [31]. Reliable refractive index measurements on In$_x$Ga$_{1-x}$N are currently not available so that a linear interpolation of binary parameters is chosen here [32]. In addition, we employed the bandgap relations given in (15) and (16),

respectively. The resulting refractive index values are given in Table II.

TABLE II
LAYER STRUCTURE AND ROOM TEMPERATURE PARAMETERS

Parameters	d	μ	n_r	K_L
Unit	μm	1/cm^{2}VS	-	W/cmK
p-GaN(contact)	0.3	10	2.54	1.3
p- Al$_{0.08}$Ga$_{0.92}$N(waveguide)	0.5	1.05	2.48	0.2
p-GaN(cladding)	0.1	10	2.54	1.3
p-Al$_{0.2}$Ga$_{0.8}$N(stopper)	0.02	10	2.23	0.6
4×n- In$_{0.02}$Ga$_{0.98}$N(barrier)	0.007	850	2.61	0.7
3×n- In$_{0.15}$Ga$_{0.85}$N(QW)	0.0035	300	3	0.2
n-GaN(cladding)	0.1	410	2.54	1.3
n- Al$_{0.08}$Ga$_{0.92}$N (waveguide)	0.5	10	2.48	0.2
n- In$_{0.05}$Ga$_{0.95}$N(compliance)	0.1	390	2.55	0.7
n-GaN (substrate)	0.3	410	2.54	1.3

To obtain the numerical parameters required for k.p calculations for the AlGaN and InGaN materials, a linear interpolation between the parameters of the relevant binary semiconductors was utilized. The material parameters of the binary semiconductors are taken from the paper by Piprek and Nakamura and are summarized in Table III [28].

TABLE III
MATERIAL PARAMETERS OF THE BINARY SEMICONDUCTORS ROOM TEMPERATURE

Parameter	Symbol	Unit	InN	GaN	AlN
Lattice constant	a_0	A$^\circ$	3.548	3.189	3.112
Spin-orbit energy	Δ_{so}	eV	0.001	0.013	0.019
Crystal-field energy	Δ_{cr}	eV	0.041	0.042	-0.217
Hole effective mass parameter	A_1	-	-9.24	-7.24	- 3.95
Hole effective mass parameter	A_2	-	-0.60	-0.51	-0.27
Hole effective mass parameter	A_3	-	8.68	6.73	3.68
Hole effective mass parameter	A_4	-	-4.34	-3.36	-1.84
Hole effective mass parameter	A_5	-	-4.32	- 3.35	- 1.92
Hole effective mass parameter	A_6	-	-6.08	- 4.72	- 2.91
Hydrost. Deform. potential (c-axis)	a_z	eV	-3.5	-4.9	-3.4
Hydrost. Deform. potential (transverse)	a_c	eV	-3.5	-11.3	-11.8
Shear deform. potential	D_1	eV	-3.7	-3.7	-17.1
Shear deform. potential	D_2	eV	4.5	4.5	7.9
Shear deform. potential	D_3	eV	8.2	8.2	8.8
Shear deform. potential	D_4	eV	-4.1	-4.1	-3.9
Elastic constant	GaP	C_{33}	200	392	382
Elastic constant	GaP	C_{13}	94	100	127

Electron eff. mass (c-axis)	m^z_c	m_0	0.11	0.20	0.33
Electron eff. mass(transverse)	m^t_c	m_0	0.11	0.18	0.25

Built-in polarization induced due to spontaneous and piezoelectric polarization is known to influence the performance of nitride devices. However, according to Piprek and Nakamura studies about InGaN MQW edge emitting lasers, the rising carrier density with higher lasing power led to enhanced screening of the polarization charges. The maximum output power was the same with or without polarization [28].Therefore; we ignore polarization effects in the following of the paper.

Fig. 2 illustrates current-voltage (I-V) characteristics and the light output power per coated facet of the LD with a cavity length of 150 μm as a function of the forward current (L-I) at room temperature. No stimulated emission was observed up to a threshold current of 50 mA. The operating voltage at the threshold current was 5.5 V and the lasing wavelength of the LD was 400.2 nm [18].
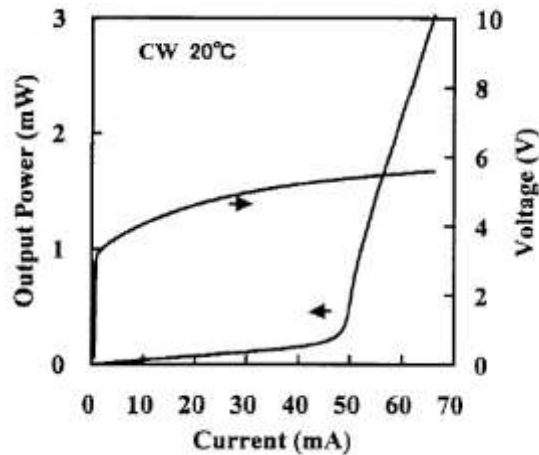
Fig. 2. Typical L–I and V–I characteristics of InGaN MQW LD's measured under CW operation at room temperature [17].

The applied drift-diffusion parameters give yield agreement with the measured current-voltage (I-V) characteristic, As seen in Fig. 3. Simultaneous agreement with the experimental light–current (L-I) characteristic and mode spectrum can be achieved by finding four fit parameters that are unknown for the mentioned device: the internal modal loss (α_i), the bandgap renormalization coefficient (ζ), the scattering relaxation time in the multi-quantum well (τ_{scat}), and the thermal resistance (R_{th}). The α_i mainly controls the slope efficiency; ζ

affects the threshold current, τ_{scat} determines the laser wavelength, and R_{th} has a major impact on the power roll-off. The values $\alpha_i = 12$ cm^{-1}, $\zeta = 1.75 \times 10^{-10}$ eVcm, $\tau_{scat} = 0.15$ ps, and $R_{th} = 75$ K/W reproduced excellent L-I curve compared with the measured data.
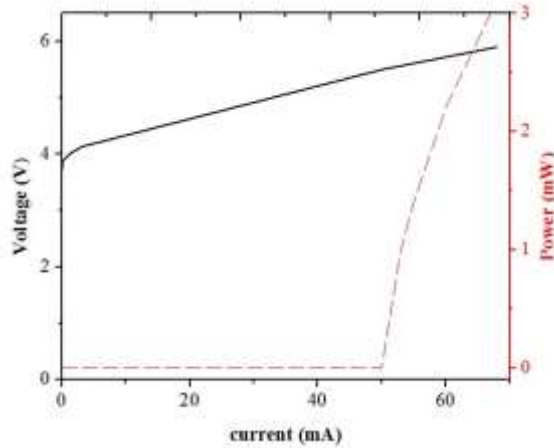

Fig. 3. Simulated L-I and I-V characteristics at CW operation for stage temperature of 20°C.

   Fig. 3 shows simulated L-I and I-V characteristics at CW operation for the 20°C stage temperature. By comparing Fig. 2 and Fig. 3, we notice that a good agreement exists between simulation and experimental results. Through the simulation, the threshold current and threshold voltage were obtained 50 mA and 5.5 V, respectively.

4. DISCUSSIONS OF THE RESULTS OF SIMULATION

   According to the good agreement with measurements, one can use the simulation results to analyze quantitatively the laser diode performance. The importance of the energy band diagram for the semiconductor laser is attributed to the fact that many important physical and optical properties of the device can be explained using its energy bandgap. The energy band diagram near the QW active in Fig. 4 further explains the difficulty of hole injection into QWs using a 0.5 μm thick layer of p-type Al$_{0.08}$ Ga$_{0.92}$ N as an electron blocking layer in the conventional laser. The diagram is obtained at room temperature with an applied current of 70 mA. The left-hand side of the diagram shows the n-side of the device, and the dashed lines represent the quasi-Fermi levels. It is shown that the high-bandgap Al$_{0.08}$ Ga$_{0.92}$ N layer was on the p-side of the QW active region. In addition, because the electrons have a higher mobility than the holes,

the $Al_{0.08} Ga_{0.92} N$ layer can act as an electron-blocking layer to prevent electron leakage and hence improve the laser performance at high current injection. In addition, there is an evident potential dip at the interface between the last quantum barrier and EBL, which is located above the electron quasi Fermi level and thus enhance the electron density on the left-hand side of the EBL. However, the increased barrier height in the valence band would result in the difficulty of hole injection into QWs when the device is at a lower current injection and therefore the threshold current increases [20].
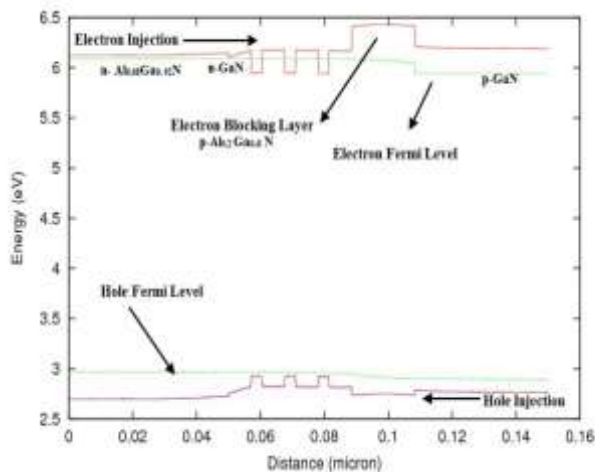
Fig. 4. Energy band diagram near the QW active region of the conventional laser at 70 mA.

It is apparent that in the nitride laser**,** the p-cladding layer can be applied to confine injected electrons, but only if it is placed in close proximity to the MQW active region [17]. As the next step of our study, the laser with new waveguide structure was simulated. In the new structure, the p-type $Al_{0.2} Ga_{0.8}$ N electron blocking and p-type GaN layers were removed and the other parts of the conventional laser structure remained unchanged. The energy band diagram of the new laser is illustrated in Fig. 5. Fig. 5 confirms that the energy band in the new structure was more suitable for hole injection since the valence band was smoother compared to the conventional structure, thus the hole injection efficiency was improved evidentially. As depicted in Figs. 4 and 5, the new waveguide structure had no effect on band energy at the interface between the n-waveguide layer and the first quantum well, which did not prevent electrons from injecting into the active region in the new laser structure.
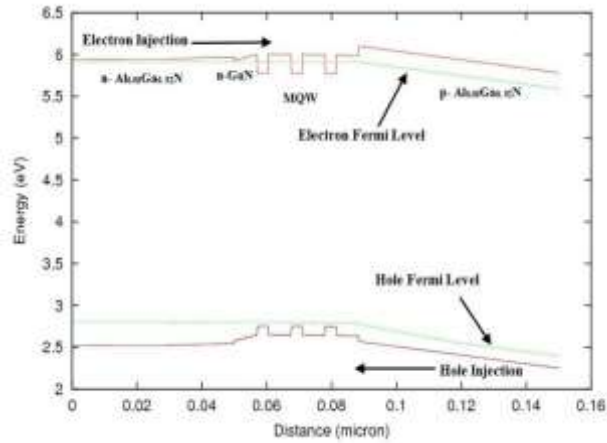
Fig. 5. Energy band diagram near the QW active region of the new laser at 70 mA.

The simulated vertical hole current density profiles of the two structures near the active region at 70 mA are illustrated in Fig. 6. For conventional structure, the hole current density before the active region was about 2600 A/cm^2, which indicated that there existed serious problem on the hole injection current. For the new structure, hole current density before the active region was about 2750 A/cm2. It means that the hole injection occurred more effectively in the new structure due to the barrier destruction near the p-side of MQWs in the hole path in the valence band. Form another point of view, in the valence band of conventional structure, there was a low energy point at the interface between the last quantum barrier and EBL where holes could accumulate. This band bending situation did not exist at the interface between the last quantum barrier and EBL in new structure, thus more holes could directly move into the MQW from the p-type region and thus hole current density increased. It was also noted that the reduction of hole current density became larger from p-side to n-side since it more carriers distributed and recombined in the quantum well near the n-side of laser diodes. For conventional structure, the reduction of hole current density was larger than that of the new structure.
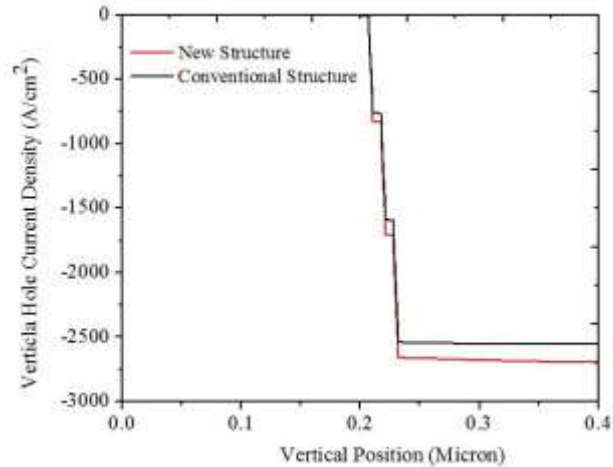
Fig. 6. Hole current density of conventional structure and the new structure at 70 mA.

The calculated new and conventional quantum well hole distributions are shown in Fig. 7. It can clearly be seen that for both structures, the profiles of the hole distributions were almost the same except that the hole concentration in new structure was higher than that in conventional structure due to the near-zero hole barrier height compared with the conventional structure and the increasing of hole current density. In addition, holes tended to accumulate in the last quantum well close to the p-side of both laser structures, and the hole concentration in the quantum wells was gradually decreased in the conventional structure and new structure from the p- to the n-side because of their large effective mass and low mobility. The uniform distribution of holes has been seen in both MQW of LDs.
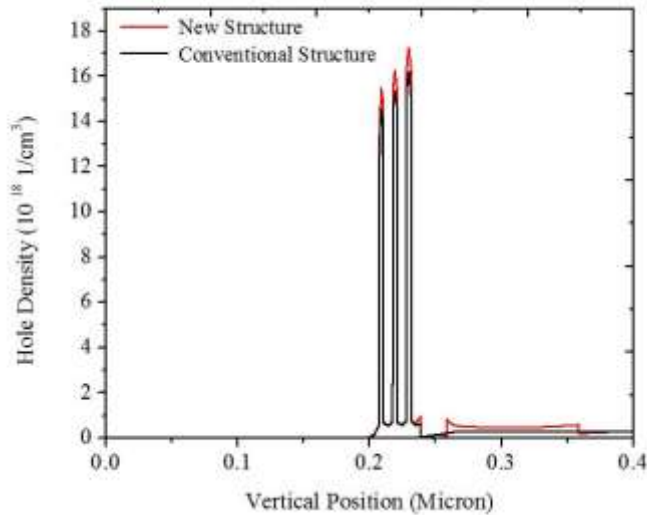
Fig. 7. Hole density of conventional structure and the new structure at 70 mA.

Next, the effect of removing the electron blocking layer on electron concentration was investigated. Fig. 8 compares the simulated electron density of two structures. It is expected that by removing the EBL, the electrons' escape from the active region increases and electron density decreases in MQWs. But, Fig. 8 shows an evident accumulation of electrons in the MQW for both LDs. This means that the electrons had the same confinement conditions in our new proposed structure. For both LDs, electrons tended to accumulate in the first and last QWs, with most electrons confined in the last QW near the p-sides of LDs due to strong electron confinement in the last QW.
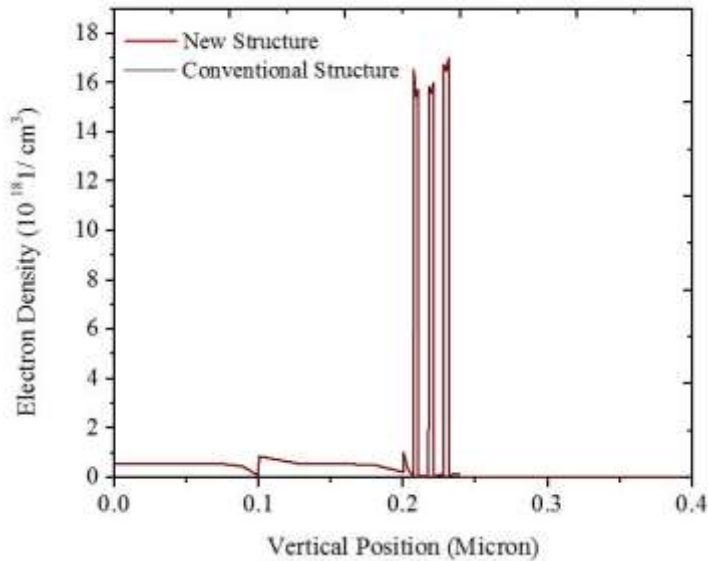
Fig. 8. Electron density of conventional structure and the new structure at 70 mA.

It is well known that the electric properties of LD determine the device optical behavior. Stimulated recombination rate has a critical role in the LD optical performance. The stimulated recombination rates of the devices are displayed in Fig. 9. As it's expected, the rate of stimulated recombination in the new structure was much larger than that of the other device. Since the hole injection efficiency was improved evidentially in the new structure and more holes were accumulated within the MQW active region and recombined with electron.
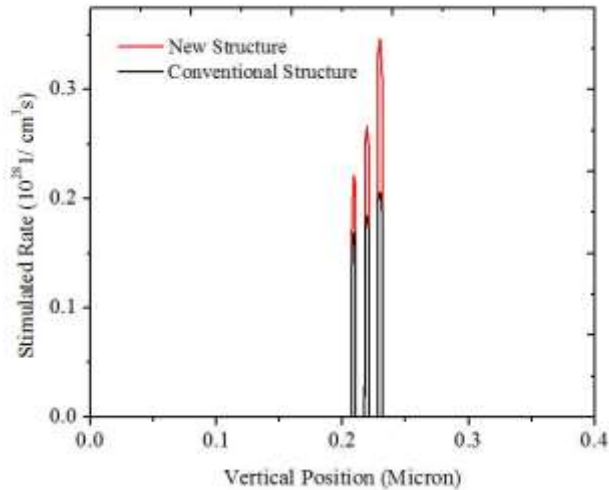
Fig. 9. The stimulated rate of the conventional structure and the new structure at 70 mA.

All wells contributed to the stimulated emission because of the uniform carrier distribution in the QWs, which results in the small efficiency droop of both structures. On the other hand, the QWs located close to the p-side layers made a major contribution to stimulated recombination due to more accumulation of carriers. In the new LD structure, since the stimulated recombination in each QW was enhanced compared with that in the conventional LD, as a result, its optical performance improved correspondingly.

The optical gain arises from the stimulated recombination of electrons and holes within the MQWs. Fig. 10 compares the local gain of the new and the conventional structures. The optical gain was observed to increase gradually from n- sides to p-sides for both LD structures because of more stimulated recombination rates of carriers.
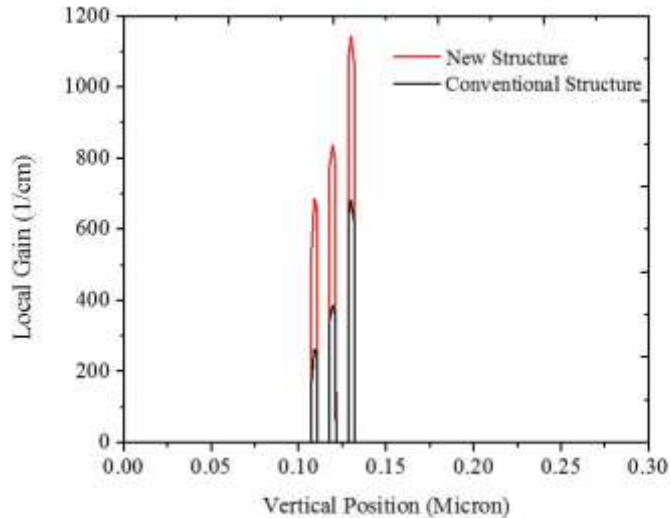
Fig. 10. The local gain of the conventional structure and the new structure at 70 mA.

Two very important factors in determining LD performance are optical loss and overlapping of optical mode and MQW active region. Refractive index profiles and resulting optical modes profile and overlap with central gain mediums in the conventional laser structure and the new laser structure are represented in Figs. 11 and 12, respectively.
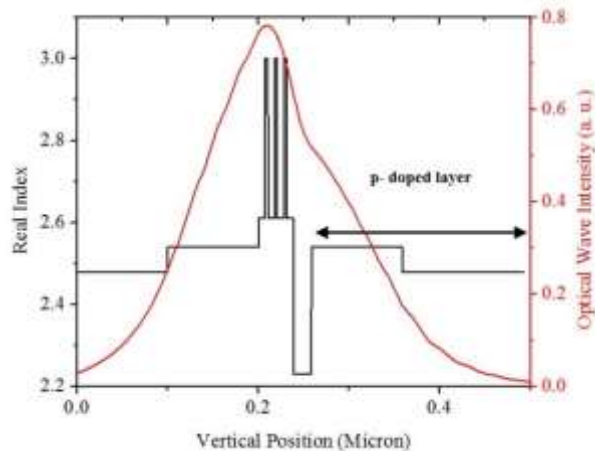

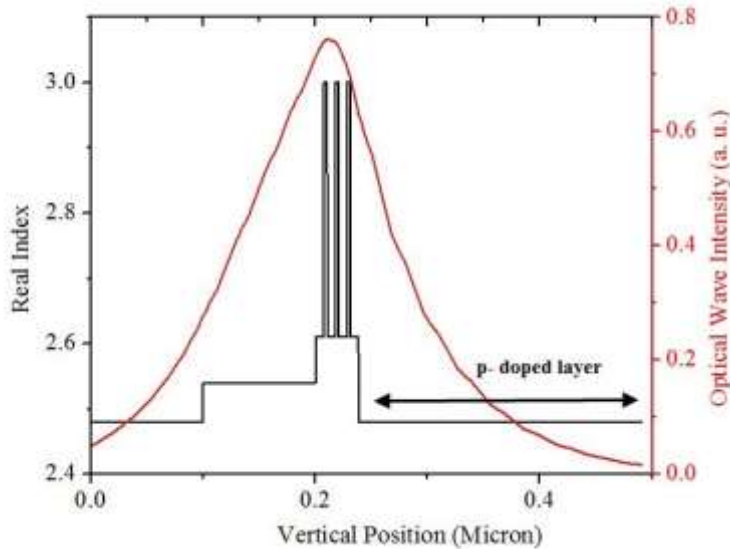**Fig. 11**. Refractive index profile and an optical mode in the conventional structure.

Fig. 12. Refractive index profile and an optical mode in the new structure.

The internal optical loss consists of cladding, waveguide, and active region loss. Since long cavity is essential in the semiconductor laser structure to increase the gain for a high power operation. The waveguide must be designed with the allowable loss, which enables a significant increase in cavity length without sacrificing the efficiency. One way to reduce the internal loss is engineering the waveguide design. Shifting the optical mode to n-cladding can decrease the cladding loss since electrons have a smaller free carrier absorption cross section than holes. Meanwhile, active region loss can be reduced since the optical mode overlaps less with the gain region [33]. In the conventional structure, using the p-doped AlGaN layer over the MQW had a significant effect on the mode profile (Fig. 11). Such a low-index layer inserted next to the QW's tended to distort the mode. The overlap of the p-doped layer with the maximum optical mode was noticeable. In the new LD, the overlap between the active region and the optical mode did not change significantly compared with the conventional structure while the overlap between the p-doped layers and maximum optical intensity decreased significantly.

Self-heating has a major effect on the semiconductor device performance. It leads to temperature rise of laser diode. The raised internal temperature due to current injection, limits the maximum output power because of the increase of nonradiative carrier recombination and the spread of the gain spectrum. The main heat source in the laser diode is Joule heat. In semiconductor lasers, carriers move from higher electrostatic potential to lower potential and the

corresponding energy difference is typically absorbed by lattice as Joule heat [27]. To reduce device self-heating, the waveguide is designed asymmetrically for low internal loss. Fig. 13 presents the Joule heating distribution in the conventional and the new laser structure. As can be seen, the Joule heating power density in the new structure decreased slightly. The main reason for Joule heating decreasing was the elimination of highly p-doped EBL.
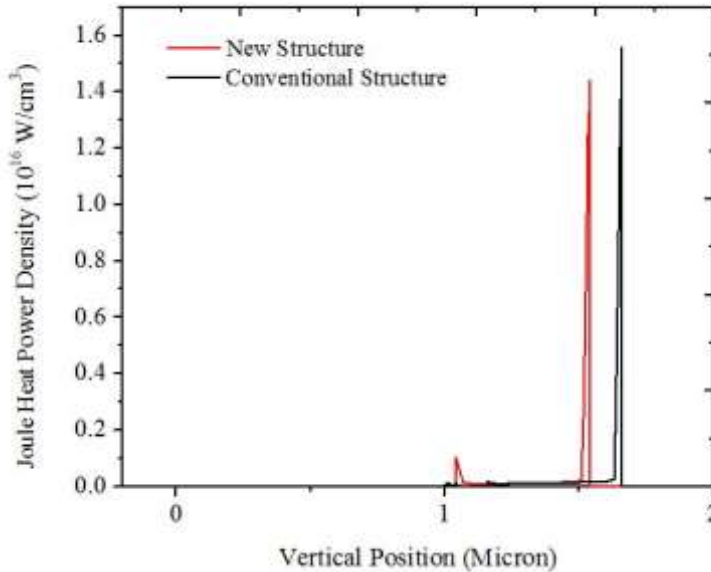

Fig. 13. Joule heat power density the conventional structure and the new structure at 70 mA.

L-I and I-V curves of the conventional and new structures are presented in Figs. 14 and 15, respectively. As can be noted, the EBL elimination and using of new waveguide design resulted in the improved InGaN MQW laser performance. Threshold current and resistance decreased using new waveguide structure. Moreover, output power and slope efficiency increased significantly.
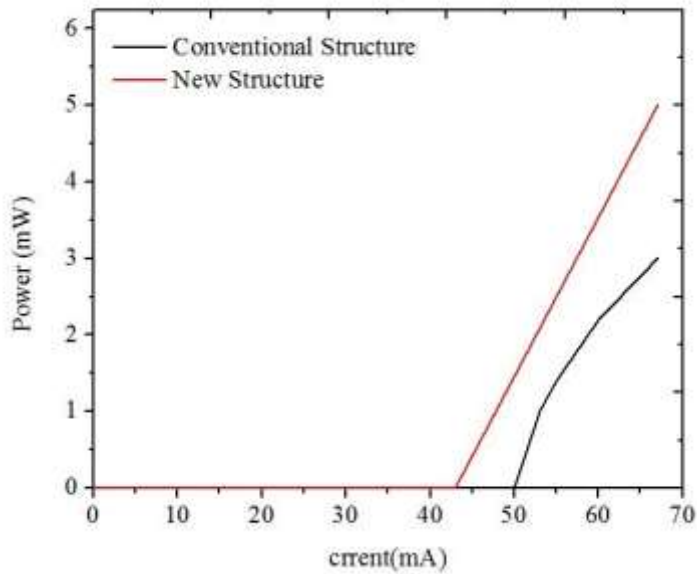
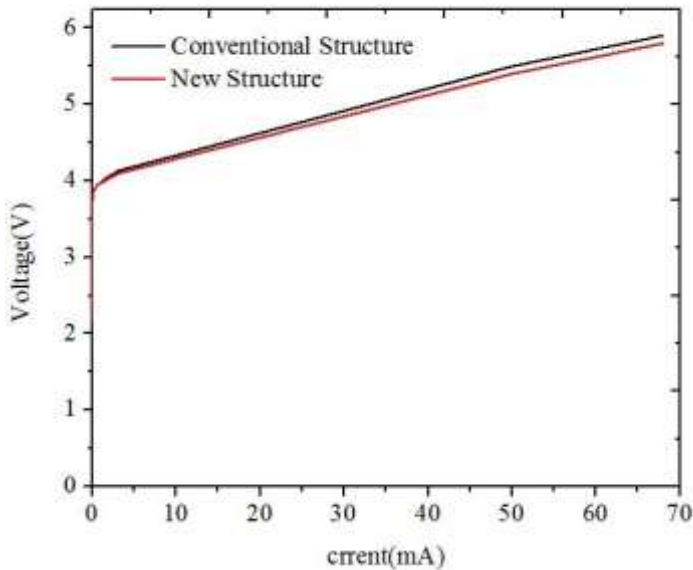**Fig. 14**. Continuous-wave optical light output power vs current at 20℃ stage temperature.

Fig. 15. Voltage vs current at a 20℃ stage temperature.

As discussed earlier, using the new waveguide structure led to increasing

stimulated recombination rate and, as a consequent, the increasing in the local gain. Such an increase is the main reason for the improvement of the new structure L-I characterization. Highly p-doped EBL was a resistive layer, thus its elimination resulted in a decreasing of the new structure operating voltage.

5. CONCLUSION

In this work, the effects of waveguide design changes on the InGaN laser diode performance was investigated theatrically using the simulation PICS3D software, which self-consistently combines 3D simulation of carrier transport, self-heating, and optical wave-guiding. Calibration of material parameters in the physical model caused an excellent agreement with measured results. After ensuring the material parameters correctness, the conventional waveguide design was changed. In the new waveguide, the p-cladding layer was used to confine injected electrons. This structure represents a departure from conventional nitride laser diode structures, where electron confinement was provided by an AlGaN barrier layer placed over the MQW active region. Numerical simulation results demonstrated that this waveguide structure efficiently increased the output power, lowered the threshold current, and improved the slope efficiency. Flatten bandgap in the p-side of the InGaN laser diode in new laser structure resulted in an increase in hole current density in the quantum well while in the same time the electron confinement in the active region was effectively created. Therefore, the stimulated recombination rate increased. In addition, the overlap of optical mode with heavily p-doped was decreased, which is the main reason for the better performance of InGaN laser diode.

REFERENCES

[1]   Y. Yang, Y. Zeng. *Enhanced performance of InGaN light-emitting diodes with InGaN/GaN superlattice and graded-composition InGaN/GaN superlattice interlayers*. Phys. Status Solidi A. 211 (7) (2014) 1640–1644.

[2] L. Cheng and S. Wu. P*erformance enhancement of blue InGaN light-emitting diodes with a GaN AlGaN–GaN last barrier and without an AlGaN electron blocking layer*, IEEE Journal of Quantum Electronics. 50 (4) (2014).

[3] M. Alias, A. Al-Omari, F. Maskuriy, F. Faiz, and S. Mitan. *Optimisation of optical properties of a long-wavelength GaInNAs quantum-well laser diode*. Quantum Electronic*s*. 43 (11) (2013).

[4]   M. Gholampour, A. Abdollah-zadeh, L. Shekari, R. Poursalehi and M. Soltanzadeh. *Green Method for Synthesizing Gallium Nitride Nanostructures at Low Temperature.* Journal of Optoelectronical Nanostructure. 3 (2018) 51-64.

[5]   A. Paliwal, K. Singh and M. Mathew, *Hole injection enhancement in InGaN laser diodes*, International Conference on Fiber Optics and Photonics, IIT, New Delhi, India, (2018) Dec. 12-15.

[6]   M. Mahbub Satter, *Design and theoretical study of wurtzite III-N deepultraviolet edge emitting laser diodes*, Ph.D. Dissertation, Georgia Institute of Technology (2014).

[7]   B. C. Lin, K. J. Chen, C. H. Wang, C. H. Chiu, Y. P. Lan, C. C. Lin, P. T. Lee, M. H. Shih, Y. K. Kuo, H.C. Kuo. *Hole injection and electron overflow improvement in InGaN/GaN light-emitting diodes by a tapered AlGaN electron blocking layer*. Optics Express. 22 (2014) 463.

[8] M. Tangi, P. Mishra, B. Janjua, A. Prabaswara, C. Zhao, D. Priante, J. W. Min, T. Khee Ng, and B. S. Ooi. *Role of quantum-confined stark effect on bias dependent photoluminescence of N-polar GaN/InGaN multi-quantum disk amber light emitting diodes*. Journal of Applied Physics. 123 (2018) 105702.

[9] S. Zhu, J. Wang, J. Yan, Y. Zhang, Y. Pei, Z. Si and J. Li, *Influence of AlGaN electron blocking layer on modulation bandwidth of GaN-based light emitting diodes*. ECS Solid State Letters. 3 (2014) R11.

[10]   A. X. Li, C. L. Mo, J. L. Zhang, X. L. Wang, X. M .Wu, G. X. Wang, F. Y. Jiang. *Effect of Mg-preflow for p-AlGaN electron blocking layer on the electroluminescence of green LEDs with V-shaped pits.* Chinese Physics Letters. 3 (2018) 027301.

[11] Z. H. Zhang, S. W. Huang Chen, C. Chu, K. Tian, M. Fang, Y. Zhang, H. C. Kuo. *Nearly efficiency-droop-free AlGaN-based ultraviolet light-emitting diodes with a specifically designed super lattice p-type electron blocking layer for high Mg doping efficiency*. Nanoscale Research Letters. 13 (2018) 1.

[12] T. Kolbe, A. Knauer, J. Rass, H. K. Cho, S. Hagedorn, S. Einfeldt, M. Kneissl and M. Weyers. *Effect of electron blocking layer doping and composition on the performance of 310 nm light emitting diodes*. Materials. 10 (2017) 1396.

[13] J. Piprek. *Analysis of efficiency limitations in high-power InGaN/ GaN laser diodes*. Opt. Quant. Electron. 48 (2016) 471.

[14]   N. Tetsuo, I. Nobuyuki, T. Kazuyoshi , K. Keita and K. Tetsu. *Wide range doping control and defect characterization of GaN layers with various Mg concentrations*. Journal of Applied Physics. 124 (2018) 165706.

[15]   B. Zhu, Z. H. Zhang, S. T. Tan, S. Lu, Yi. Zhang, X. Kang, N. Wang, N. Hasanov, H. V. Demir. *Effect of Mg doping in the barriers on the electrical performance of InGaN/GaN-based light-emitting diodes*. Physica E: Low-dimensional Systems and Nanostructures. 98 (2018) 29.

[16] P. Chen, C. H. Kuo, W. C. Lai, Y. A. Chen, L. Chang and S. Chang. *GaN-based light-emitting-diode with a p-InGaN layer*. Journal of Display Technology. 10 (3) (2014) 204-207.

[17]   X. Li, D. Zhao, D. Jiang, P. Chen, Z. Liu, Ji. Zhu, M. Shi, D. Zhao and W. Liu *Suppression of electron leakage in 808 nm laser diodes with asymmetric waveguide layer*. Journal of Semiconductors. 37 (1) (2016) 014007.

[18]   S. Nakamura. *InGaN-based blue laser diodes*. IEEE Journal of Selected Topics in Quantum Electronics. 3 (3) (1997) 712-718.

[19] D. H. Hsieh, A. J. Tzou, T. S. Kao, F. I. Lai, D. W. Lin, B. C. Lin, T. C. Lu, W. C. Lai, C. H. Chen and H. C. Kuo. *Improved carrier injection in GaN-based VCSEL via AlGaN/GaN multiple quantum barrier electron blocking layer*. Optics Express. 23 (2015) 27145.

[20]   M. Xia, H. Ghafouri Shiraz. *Analysis of carrier heating effects in quantum well semiconductor optical amplifiers considering holes' Non-parabolic density of states*. Optical and Quantum Electronics. 47 (7) (2015) 1847-1858.

[21] M. Re. Jalal and M. Habibi. *Simulation of Direct Pumping of Quantum Dots in a Quantum Dot Laser. Journal of Optoelectronical Nanostructure. 2 (2017) 61-69.*

[22] M. Riahinasab and E. Darabi. *Analytical Investigation of Frequency Behavior in Tunnel Injection Quantum Dot VCSEL.* Journal of Optoelectronical Nanostructure. 3 (2018) 65-75

[23]   H. Bahramiyan and S. Bagheri. *Linear and nonlinear optical properties of a modified Gaussian quantum dot: pressure, temperature and impurity effect*. Journal of Optoelectronical Nanostructure. 3 (2018) 79-99.

[24] J. Piprek. *Internal power loss in GaN-based lasers: Mechanisms and remedies*. Opt. Quant. Electron. 49 (2017) 329.

[25] G. Kyritsis and N. Zakhleniuk. *Self-consistent simulation model and enhancement of wavelength tuning of InGaAsP/InP multisection DBR laser diodes*. IEEE Journal of Selected Topics in Quantum Electronics. 19 (5) (2013).

[26]   V. S. Volcheck, V. R. Stempitsky, *Suppression of the self- heating effect in GaN-HEMT by few layer graphene heat spreading elements*. Journal of Physics: Conf. Series. 917 (2017) 082015.

[27] Z. Danesh Kaftroudi, E. Rajaei and A. Mazandarani. *Simulation of a single-mode tunnel-junction-based long-wavelength VCSEL*. Journal of Russian Laser Research. 35 (2) (2014) 124-137.

[28]   J. Piprek and S. Nakamura. *Physics of high-power InGaN/GaN lasers*. IEE Proc.-Optoelectron. 149 (4) (2002) 145-151.

[29] T. Wang, J. Xu, X. Wang. *Self-heating dependent characteristic of GaN-based light-emitting diodes with and without AlGaInN electron blocking layer*. Chin. Sci. Bull. 59 (20) (2014) 2460–2469.

[30]   S. Salimpour and H. Rasooli Sagha. *Impressive Reduction of Dark Current in InSb Infrared Photodetector to achieve High Temperature Performance*. Journal of Optoelectronical Nanostructure. 3 (2018) 81-95.

[31] L. A. M. Sulmon, *Static and dynamic characteristics of InGaN-based laser diodes,* Phd Thesis, LASPE (2014).

[32] J. Piprek and Z. M. Li. *Electroluminescent cooling mechanism in InGaN/GaN light-emitting diodes*. Opt. Quant. Electron. 48 (2016) 472.

[33] B. S. Ryvkin, E. A. Avrutin and J. T. Kostamovaara, *Optical loss suppression in long-wavelength semiconductor lasers at elevated temperatures by high doping of the n-waveguide.* Semicond. Sci. Technol. 33 (2018) 105010.